ISSN 2007-9737

Radiometric Cross-Calibration of Low-Cost Multispectral and Hyperspectral Sensors under Variable Sun-Sensor Geometry for UAV Remote Sensing Applications

Azgad Casiano Ramos[1,*], Maria Dolores Guevara Espinosa[2], María de los Ángeles Velasco Hernández[3], María Catalina Rivera Morales[2], Ana Claudia Zenteno Vázquez[4], María del Carmen Santiago Díaz[4], Gustavo Trinidad Rubín Linares[4], Luis Alberto Morales Rosales[5]

[1] Benemérita Universidad Autónoma de Puebla, Faculty of Electronic Sciences, Mexico

[2] Benemérita Universidad Autónoma de Puebla, Faculty of Chemical Engineering, Mexico

[3] Benemérita Universidad Autónoma de Puebla, Institute of Sciences – Zeolites Research Department, Mexico

[4] Benemérita Universidad Autónoma de Puebla, Faculty of Computing Sciences, Mexico

[5] Conahcyt – Hidalgo's Michoacan University of San Nicholas (UMSNH), Mexico

azgad.casianor@alumno.buap.mx, {dolores.guevara, angeles.velasco, maria.riveram, ana.zenteno, marycarmen.santiago, gustavo.rubin}@correo.buap.mx, lamorales@conahcyt.mx

Abstract. In this work, the radiometric cross-calibration of low-cost multi/hyperspectral sensors for UAV remote sensing applications with consideration of sun-sensor geometry effects is investigated. First, the standard BRDF model is used to deduce the radiometric correction factors associated to the sun-sensor geometry. Then, the LRM model is used to calibrate the hyperspectral measurements from the corrected multispectral ones. In order to test this methodology, an agriculture-type UAV with integrated multispectral camera and a point micro-spectrometer are used. Results of the corrected irradiance based calibration in a set of four reference targets under clear sky conditions show a reduction of up to 1:3 in the mean absolute reflectance estimation error (MAE) with respect to the reflectance based calibration without irradiance normalization.

Keywords. UAV, remote sensing, multispectral, hyperspectral, sun-sensor geometry, cross-calibration, reflectance, workflow.

1 Introduction

Consistent and accessible radiometric correction methods are fundamental for the development and adoption of new remote sensing applications using spectral sensors on board Unmanned Aerial Vehicles (UAVs), such as smart agriculture (Iqbal et al., 2018), mineral exploration (Jakob et al., 2017) and environmental monitoring (Manfreda et al., 2018), among others. In the last years, several methods for radiometric correction

applicable to remote sensing using UAVs have been proposed (Li et al., 2015; Aasen et al., 2018; Hakala et al., 2018; Guo et al., 2019; Daniels et al., 2023). Generally, the goal of the calibration process is to estimate the reflectance of an observed surface, since it is a physical parameter independent of the illumination intensity (Peddle et al., 2001). It can be used to create high spatio-temporal resolution maps enhanced with spectral information, such as spectral indices associated to biophysical or physicochemical parameters (Cohen et al., 2019). Nevertheless, reflectance estimation is prone to instrumental and atmospheric related errors (Burkart et al., 2014; Köppl et al., 2021). According to the Bidirectional Reflectance Distribution Function model (BRDF) proposed by Nicodemus in 1977, reflectance of a surface is a function of the observation angle, thus, a lot of research has been focused on reflectance estimation by considering angular effects such as sensor tilting (Burkart et al., 2015; Köppl et al., 2021), sun-sensor geometry (Roosjen et al., 2017; Jafarbiglu et al., 2023) and terrain topography (Yu et al., 2024).

A single spectral sensor is unable to capture all the ranges of spectral information, hence sensor cross-calibration is used to combine spectral measurements of different scales into common units to harness the spatio-temporal resolution, spectral range or field of view of different spectral sensors (Li et al., 2024). Recently, the miniaturization of hyperspectral sensors has opened a new field for the development of high throughput spectrometry on board UAVs (Burkart et al., 2014; Adão et al., 2017; Aasen et al., 2018; Köppl et al., 2021). Particularly, fusion of multispectral (MS) and hyperspectral (HS) imaging has been mainly reported in the literature (Yokoya et al., 2017; Brezini et al., 2023; Samadzadegan et al., 2025). However, literature on cross-calibration of multispectral imagers and low cost point spectrometers is scarce (Zeng et al., 2017; Natesan et al., 2018).

Radiometric correction workflows for UAVs remote sensing can be reflectance, irradiance or radiance based (Chen et al., 2021). The first requires synchronous reflectance measurements from reference panels on ground and the introduction of atmospheric parameters to the radiative model in order to obtain the radiance to reflectance calibration curve at sensor level under the low aerosol loading assumption. Irradiance based method improves the reflectance method by adding synchronous ground level irradiance measurements for the computation of the diffuse to global ratio, reducing its sensibility to the aerosol loading. The radiance based workflow requires the use of a laboratory calibrated spectroradiometer for absolute radiance measurements at the UAV level under the same viewing conditions of the uncalibrated sensor (Chen et al., 2021).

The implementation of the all the aforementioned workflows is logistically and technically complex due to the requirement of synchronous measurements on the ground and and in the air: the quantity of reference panels necessary to cover the spectral range or the extension of the study area can be limited, a gold standard field spectroradiometer is a sophisticated equipment whose cost may be prohibitive, the use of a low cost spectrometer for absolute radiance measurements require complex laboratory calibration methods that can be invalidated by optical system changes (Ocean Optics Inc., 2007). Therefore, calibration data is often taken only at the start and at the end of the flight mission (Olsson et al., 2021). In other cases, the use of reference panels is avoided and substituted by reflectance factors computed from on board irradiance sensors (Cubero-Castan et al., 2018; Hakala et al., 2018; Schneider-Zapp et al., 2019). By the other hand, the radiometric correction process developed by (Micasense, 2017) is a workflow developed for the industry, with combined features of the three types of workflows, harnessing the UAV integrated navigation sensors and enabling advanced users to implement their own workflows.

In remote sensing applications on board UAVs where the sun is used as light source, the sun-sensor geometry is an important influencing factor on reflectance estimation and its derived products such as the spectral indices (Burkart et al., 2015; Jafarbiglu et al., 2023; Wang et al., 2023). Several authors have addressed the issue of variation of spectral indices with changing illumination conditions by its evaluation and selection according to its robustness in specific applications (Stow et al., 2019)(Sun et al., 2021) or by designing ad hoc spectral indices (Graham et al., 2022). Nevertheless, the integration of the sun-

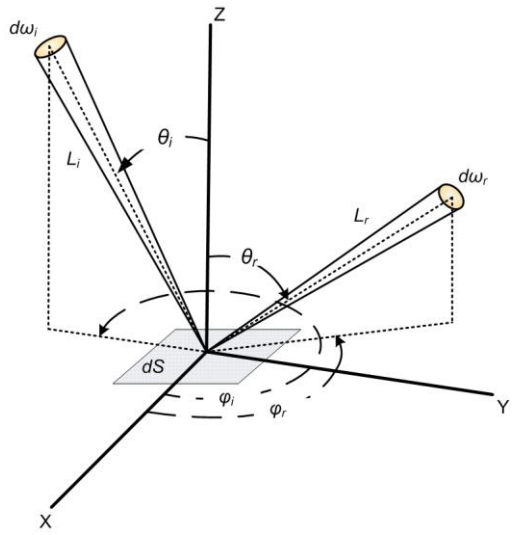

Fig. 1. BRDF model (redrawn from (Horn et al., 1979))

sensor geometry to the workflow will systematically improve the reflectance estimation through radiometric correction factors for estimating, for instance, the at-surface sun irradiance (Köppl et al., 2021; Micasense, 2022).

In (Zeng et al., 2017) a method to simulate HS imaging by fusion of MS imagery and HS spectral data from a spectrometer is proposed. There, reflectance is estimated as a reflectance factor with respect to a blank reference before and after the flight and the spatio-temporal alignment is made by optimizing the intensity correlation between the MS and HS data. The resulting data fusion with an R^2 from 0.72 to 0.95 and MAE of 17% was used to estimate a narrowband vegetation index. In (Natesan et al., 2018), RGB images and spectrometer data were used for classification of different land cover elements. Instead of estimating reflectance, the authors used a laboratory calibrated spectrometer in spectral exposure units ($Jm^{-2}nm^{-2}$).

The classification allowed to generate a segmentation map by land cover types with an accuracy of 50 to 78%. By the other hand, in (Köppl et al., 2021) a laboratory calibrated hyperspectral camera and downwelling light sensor (DLS) on board a UAV are used to estimate surface reflectance with irradiance correction associated to sensor tilting due to UAV displacement and estimation of the diffuse fraction due to intermitent clouds. Variations in the irradiance caused by different types of movements of the UAV were reduced up to71 and 87%, significantly lowering the striping effect in the HS reflectance factor maps.

In this article, an extension of the Micasense radiometric correction workflow (Micasense, 2022) is proposed by applying it to the cross-calibration of the Parrot Sequoia+ multispectral imager (Parrot Group, SA, Paris, FR) and the Oceanoptics STS-VIS hyperspectral point spectrometer (Ocean Optics, Inc, Orlando, FL, US).

Additionally, the sun-sensor geometry correction equations of this setup are derived in relation to the BRDF model in order to contribute to the general understanding of the radiometric correction process including the sun-sensor geometry. The aim of this implementation is to contribute to the diversification of UAV remote sensing applications by using low cost multispectral and hyperspectral sensors.

This article is developed as follows. In Section 1 the importance of radiometric calibration for UAV based remote sensing applications and some related issues are described. Also some background on reflectance estimation workflows reported in the literature is presented in relation to the cross-calibration of MS and HS data with consideration of sun-sensor geometry effects. In Section 2 the preliminary methods and the derivation of the reflectance calibration equations are given. Also, the experimental setup and the radiometric correction workflow are described. In section 3 the results of reflectance cross-calibration are presented and discussed. Finally, in Section 4 the conclusions on this work and actual contributions for future research are given.

2 Methods and Experimental Setup

2.1 BRDF Model

Reflectance is an adimensional quantity in the range [0,1], defined as the ratio of the radiant excitance M ($W \cdot m^{-2}$) and the irradiance E ($W \cdot m^{-2}$) at a surface (Schaepman-Strub et al., 2006). Reflectance modeling start from the standard BRDF function, denoted by f_R in Eq. (1) (Horn et al., 1979):

$$f_R(\theta_i, \varphi_i; \theta_r, \varphi_r) = \frac{dL_r(\theta_i, \phi_i; \theta_r, \phi_r)}{dE_i(\theta_i, \varphi_i)} [\text{sr} - 1]. \quad (1)$$

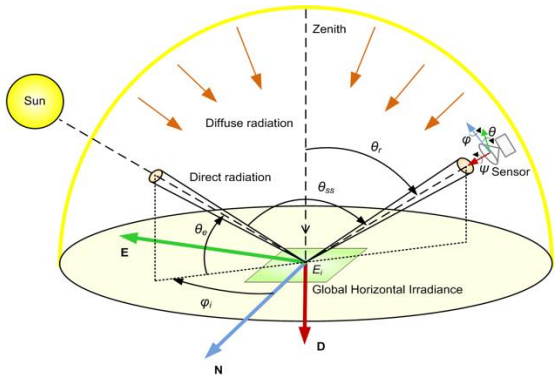

Fig. 2. Sun-sensor geometry in NED (North-East-Down) coordinates

where dL_r [W·m⁻2·sr⁻¹] is the radiance of the beam reflected by the surface *S* in the direction (θ_r, ϕ_r) through the infinitesimal solid angle $d\omega_r$ and dE_i is the irradiance on the surface due to the source beam of radiance L_i incident in the direction (θ_i, ϕ_i) through the infinitesimal solid angle $d\omega_i$. If the notation $d\Omega$ is used for te projection of the solid angle $d\omega$ on the surface normal, then $d\Omega_r = d\omega_r \cos\theta_r$ and the radiant excitance of the surface S can be calculated from $L_r$as (Horn et al., 1979):

$$M = \int_{\Omega_r} L_r d\Omega_r = \int_{-\pi}^{\pi}\int_{0}^{\pi/2} L_r(\theta_r, \varphi_r) \cos\theta_r \sin\theta_r \, d\theta_r d\varphi_r = L_r(\theta_r, \varphi_r)\pi \ [\text{W·m}^{-2}]. \quad (2)$$

If *S* is a Lambertian (i.e., a perfectly diffuse and lossless) surface, then L_r will be isotropic (i.e., equal in all directions), E_i will be equal to M and the following relation will be hold (Horn et al., 1979):

$$f_{r(Lambert)} = \frac{L_r}{E_i} = \frac{L_r}{M} = \frac{1}{\pi} [\text{sr}^{-1}]. \quad (3)$$

Where L_r can be calculated from L_i using the next alternative form of the Lambert's cosine law (Horn et al., 1979):

$$L_r = \frac{1}{\pi}\int_{\omega_i} L_i(\theta_i, \varphi_i) \cos\theta_i \, d\omega_i \ [\text{W·m}^{-2}\text{·sr}^{-1}]. \quad (4)$$

2.2 Sun-Sensor Geometry Based Reflectance Correction

Next, the irradiance correction factors used in the Micasense Image Processing© software (AgEagle Aerial Systems, Inc, Seattle, WA, US) (MIP) will be derived from the sun-sensor geometry of Fig. 2 and put into the context of the BRDF model in order to estimate the at-surface reflectance. In the MIP setup, it is assumed that there are two multispectral sensors on board the UAV: one imaging sensor pointing to the surface and one downwelling irradiance light sensor (DLS) pointing up in an ideally opposite direction to the imaging sensor. If the orientation of the sun and the DLS sensor are given by the vectors $\hat{n}_{sun}$ and $\hat{n}_{sensor}$, respectively, the sun-sensor angle, θ_{ss}, will be given by:

$$\theta_{ss} = arccos(\hat{n}_{sun} \cdot \hat{n}_{sensor}). \quad (5)$$

where $(\cdot)$denote the dot product. By using the notation $c_{(\cdot)} = cos(\cdot)$ and $s_{(\cdot)} = sin(\cdot)$, the $\hat{n}_{sun}$ vector can be expressed in NED coordinates from the solar azimuth (ϕ_i) and elevation (θ_e) angles as (Micasense, 2017):

$$\hat{n}_{sun} = \begin{bmatrix} c_{\phi_i} c_{\theta_e} \\ s_{\phi_i} c_{\theta_e} \\ -s_{\theta_e} \end{bmatrix}. \quad (6)$$

Thus, the $\hat{n}_{sensor}$ vector in NED coordinates can be obtained from the roll-pitch-yaw XYZ angles (ϕ, θ, ψ) of an Inertial Measurement Unit (IMU) plus north reference attached to the DLS sensor frame on board the UAV as (Micasense, 2017):

$$\hat{n}_{sensor} = R_{ZYX}(-\psi, -\theta, -\phi)\hat{n}_{sensor-UAV}. \quad (7)$$

Where R_{ZYX} is the matrix of successive rotations around the Z, Y and X axes and $\hat{n}_{sensor-UAV} = [0 \quad 0 \quad -1]^T$ defines the orientation vector of the DLS sensor relative to the UAV reference frame.

At the ground level, the global hemispherical irradiance that incides on a horizontal surface can be expressed as (Kosmopoulos, 2024):

$$E_i = E_i^{dir} \sin\theta_e + E_i^{diff}. \quad (8)$$

Where k_{arb}^{irr} is a conversion factor from I^{dls} units to physical units of irradiance. Assuming that E_i^{diff} is isotropic, i.e., incident angle independent and

Table 1. Specifications of the multispectral/hyperspectral cross-calibration experimental setup components

Component	Characteristic	Specification
UAV	Wireless link type (frequencies)	Wi-Fi 802.11a/b/g/n (2,4-5,8 GHz)
Parrot Sequoia+	Multispectral band (center wavelength / bandpass)	Green (GRE) (550 nm / 40 nm) Red (RED) (660 nm / 40 nm) Red edge (REG) (735 nm / 10 nm) Near Infrared (NIR) (790 nm / 40 nm)
Parrot Sunshine	Sensor type (wavelengths)	DLS (same as Sequoia+)
Airinov MS panel	Multispectral bands (reflectance)	GRE (18.9%) RED (20.1%) REG (22.7%) NIR (26%)
Ocean Optics STS-VIS	Band (Wavelengths) / resolution	Visible (336-824 nm) / 1.5 nm

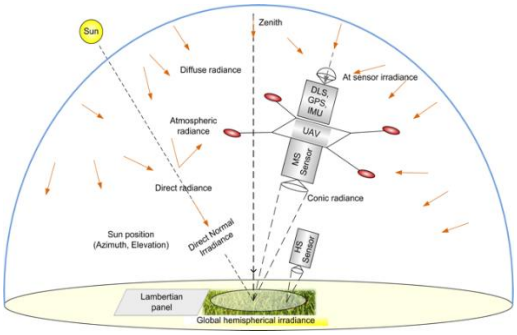

Fig. 3. Multi/hyperspectral cross-calibration setup

that L_r^{sensor} is the Lambertian surface radiance measured by the imaging sensor in arbitrary units homogeneous (α) to W·m⁻2·sr⁻¹ within an unknown solid angle, Ω_r, then the excitance of the surface can be computed as:

$$M = \pi L_r = k_{rad,arb}^{exc} L_r^{sensor}. \quad (10)$$

where $k_{rad,arb}^{exc}$ is a conversion factor from arbirary units of $L_r^{sensor}$to physical units of excitance, passing through the process of integration within the FOV of the imaging sensor. Finally, the reflectance of a target in the band Λ can be computed in terms of the sun-sensor geometry as (cf.) (Micasense, 2017; Domenzain et al., 2018):

$$\rho^{target}(\theta_{ss}, \theta_e, \kappa, \Lambda) = \frac{1}{k_\Omega(\Lambda)} \frac{(cos\,\theta_{ss} + \kappa)}{(sin\,\theta_e + \kappa)} \frac{L_r^{sensor}(\Lambda)}{I^{dls}(\Lambda)}, \quad (11)$$

where the geometric factor $k_\Omega(\Lambda) = k_{arb}^{irr}(\Lambda)/k_{rad,arb}^{exc}(\Lambda)$ can be estimated from a Lambertian reference panel of known reflectance in the band Λ, $R_{ref}^{target,Lambert}(\Lambda)$ by:

$$\tilde{k}_\Omega(\Lambda) = \frac{k_\Omega(\Lambda)\rho^{target,Lambert}(\theta_{ss}, \theta_e, \kappa, \Lambda)}{R_{ref}^{target,Lambert}(\Lambda)}. \quad (12)$$

2.3 Multispectral-Hyperspectral Reflectance Cross-Calibration Setup

The experimental setup is depicted in Fig. 3. The UAV is a Parrot Bluegrass (Parrot Group, SA, Paris, FR), with factory integration of a Parrot Sequoia multispectral imaging sensor and a Parrot Sunshine irradiance sensor pointing up in opposite direction to the Sequoia sensor.

The Sunshine sensor includes an IMU with magnetometer and a GPS (Global Positioning Sytem) unit, necessary for the computation of θ_e and θ_{ss} in equations 6 and 7. The hyperspectral sensor is an Ocean Optics STS-VIS (Ocean

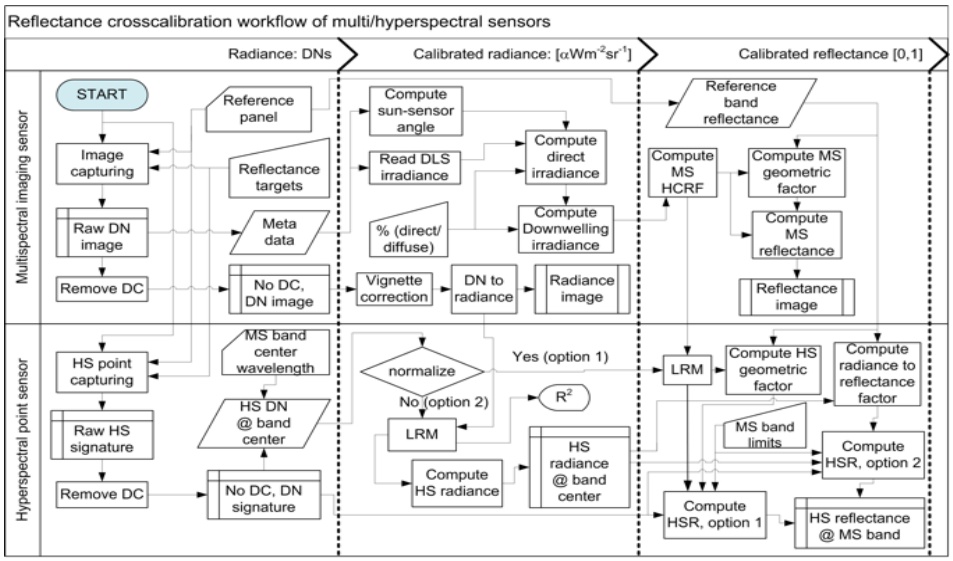

Fig. 4. Extension of the Micasense workflow to Multispectral/Hyperspectral cross-calibration

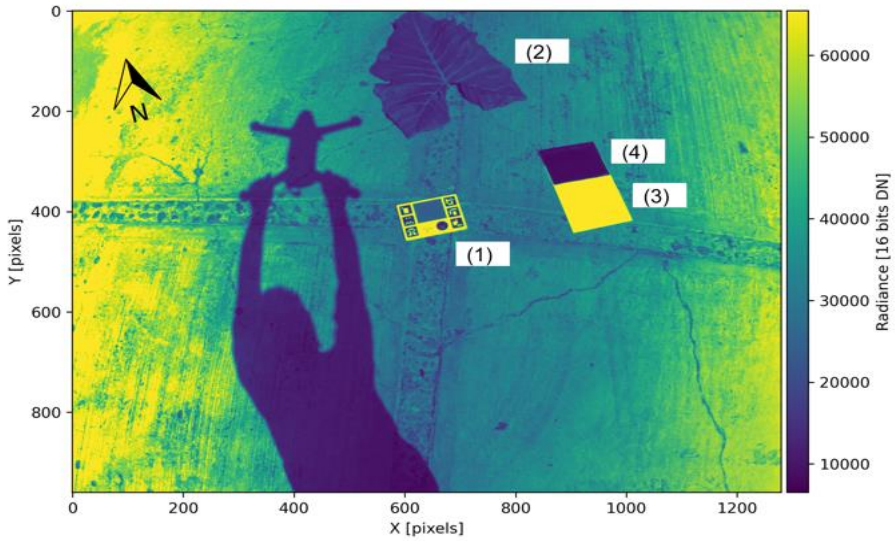

Fig. 5. Raw GREEN band image of the calibration targets in viridis false color with superimposed north arrow and target labels: (1) Airinov calibration panel, (2) *Alocasia* leaf (3) 75 g/m^2 HP® office paper (4) Airinov panel black plastic cover

Optics, Inc, Orlando, FL, US) spectrometer pointing proximaly to the ground target in order to avoid spectral mixing.

The reference target is an Airnov multispectral calibration panel (Airinov, Paris, FR) with diffuse reflectance in the same bands as the Sequoia sensor. The specifications of the aforementioned elements are presented in Table 1.

2.4 Multispectral-Hyperspectral Reflectance Cross-Calibration Workflow

The calibration process is based on the Micasense image processing workflow (Micasense, 2022) and the Micasense Image Processing© software (AgEagle Aerial Systems, Inc, Seattle, WA, US) (MIP), originally written for the RedEdge and Altum

Table 2. Cross-calibration of HS sensor from DNs to MS radiance units and to HS reflectance factor $HCRF^{HS}$

Band	$\tilde{k}_\Omega$	$\bar{e}_{ss}$ [%]	$\bar{e}_{ss}$ [%]	R^2_{nn}	R^2_{ss}
GRE	2.716	2	2	0.997	0.997
RED	2.677	6.8	4.5	0.995	0.995
REG	5.645	7.9	0.9	0.999	0.999
NIR	1.372	9.1	1.4	0.998	0.999

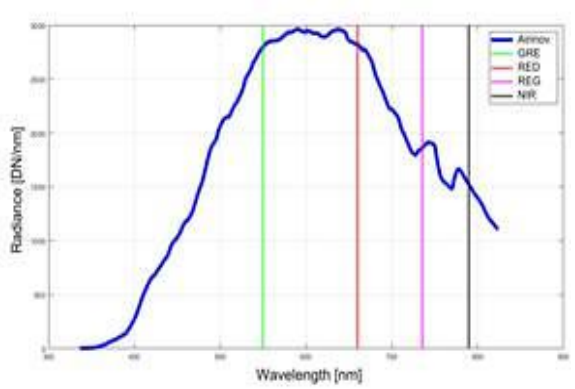

Fig. 6. HS radiance signature of the Airinov panel (DC removed) and MS central wavelengths

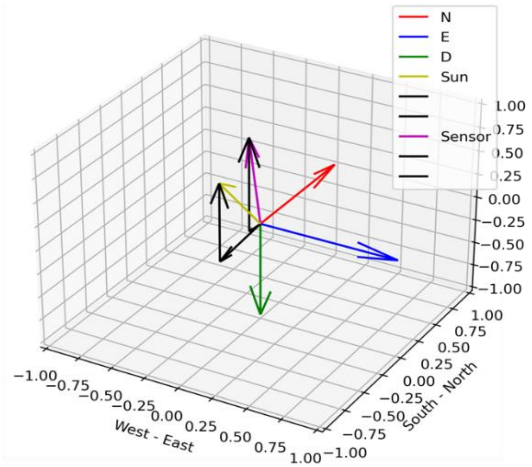

Fig. 7. Visualization of sun, sensor and NED vectors in ENU (East-North-Up) coordinates

camera models by Micasense, with added support for the Sequoia sensor by (Fenger-Nielsen, 2019). The proposed extension to the MIP workflow on a single MS band image is depicted in the simplified cross-functional flow chart of Fig. 4. In the top of the diagram, the part corresponding to MIP is presented, where some specialized blocks like lens distortion or image registration have been omitted for clarity.

In the bottom section, the extension for calibration of the HS sensor is presented, where the goal is to estimate the hyperspectral reflectance signature in a particular MS band.

2.5 Cross-Calibration via the Linear Regression Method

The Linear Regression Method (LRM) is an empirical method used in remote sensing to calibrate raw radiance measurements in sensor digital numbers (DN) to absolute reflectance values of the calibration targets assuming a linear relationship between them (Guo et al., 2019).

From Eq. 11, reflectance estimation can be seen as the normalization of the radiance reflected by a calibration target and captured by a remote radiance sensor around an unknown solid angle Ω_r with respect to the estimated irradiance at the surface level. By simplifying the notation of Eq. 13, it can also be seen as the normalization of the hemipherical-conical reflectance factor $HCRF = k_\Omega \rho^{target}$ via multiplication by $\tilde{k}_\Omega^{-1}$. The LRM method was used here to model the relationship between the raw radiance of the HS sensor, DN_L^{HS}, and the radiance in the MS band Λ as follows:

$$L_r^{MS}(\Lambda) = a(\Lambda) DN_L^{HS}(\Lambda) + b(\Lambda) + \varepsilon(\Lambda), \qquad (14)$$

where $a(\Lambda)$ and $b(\Lambda)$ can be computed by ordinary least squares method and $\varepsilon(\Lambda)$ is the residual error. Thus, the HS reflectance in the band Λ can be estimated by:

$$\tilde{\rho}^{target,HS}(\Lambda) = \tilde{k}_\Omega^{-1}(\Lambda) L_r^{HS}(\Lambda) = \tilde{k}_\Omega^{-1}(\Lambda) \left(a(\Lambda) DN_L^{HS}(\Lambda) + b(\Lambda) \right). \qquad (15)$$

3 Results

3.1 Multispectral/Hyperspectral Reflectance Cross-Calibration

The multispectral images of the calibration targets were captured on 2022-11-06 a 18:07:40-06:00 UTC/DST (Coordinated Universal Time/Daylight

Table 3. MS-HS reflectance cross-calibration: e is the reflectance error relative to the reference target. The subindices of $\tilde{\rho}^{HS}$and e indicate non-normalized (*nn*) and sun-sensor geometry (*ss*) normalized radiance used in the LRM method

Band	Target (No.)	L_r^{MS} α[W·m^{-2}·sr^{-1}]	DN_L^{HS} [10 bit counts]	L_r^{HS} [αW·m^{-2}·sr^{-1}]	$HCRF^{HS}$ [%]
GRE	(1)	17.8	2796	17.0	53.6
	(2)	10.2	1415	9.1	31.2
	(3)	54.3	9355	54.5	163.7
	(4)	4.4	885	6.1	13.1
RED	(1)	18.4	2821	17.2	48.2
	(2)	5.7	595	4.4	15.0
	(3)	73.1	9319	54.3	191.4
	(4)	3.8	905	6.2	9.9
REG	(1)	15.5	1860	11.7	129.8
	(2)	30.8	3501	21.0	258.3
	(3)	54.8	5723	33.8	460.6
	(4)	2.6	575	4.3	21.8
NIR	(1)	11.6	1549	9.9	35.0
	(2)	25.5	3127	18.9	76.9
	(3)	35.9	4078	24.3	107.0
	(4)	2.2	452	3.6	6.5

Table 4. Geometric factors by band and mean absolute HS reflectance calibration by using non normalized (*nn*) radiance and normalized by the downwelling irradiance corrected by the sun-sensor geometry (*ss*). The coefficient of determination was computed with respect to the MS-HS radiance calibration

Band	Target (No.)	$R_{ref}^{target,MS}$ [%]	$\tilde{\rho}_{nn}^{HS}$ [%]	$\tilde{\rho}_{ss}^{HS}$ [%]	$\lvert e_{nn}\rvert$ [%]	$\lvert e_{ss}\rvert$ [%]
GRE	(1)	18.9	18.9	18.9	0.0	0.0
	(2)	11	10.1	10.1	0.9	0.9
	(3)	57.7	60.6	60.6	2.9	2.8
	(4)	4.6	6.8	6.8	2.2	2.2
RED	(1)	20.1	20.1	20.1	0.0	0.0
	(2)	6.3	5.2	2.7	1.1	3.6
	(3)	79.8	63.7	70.9	16.1	8.8
	(4)	4.0	7.3	5.1	3.2	1.1
REG	(1)	22.7	22.7	22.7	0.0	0.0
	(2)	45.2	41.0	47.4	4.2	2.2
	(3)	80.6	65.7	80.8	14.8	0.2
	(4)	3.6	8.4	3.4	4.7	0.2
NIR	(1)	26.0	26.0	26.0	0.0	0.0
	(2)	57.0	49.8	57.6	7.3	0.6
	(3)	79.4	64.1	76.7	15.3	2.7
	(4)	4.8	9.5	4.0	4.7	0.8

Saving Time) at the location 19°03’29.2’’N, 98°18’25.2W’ under clear sky conditions, following the radiometric calibration image capturing procedure recommended by the UAV manufacturer (Parrot Drone, 2022) (See Fig. 5).

The hyperspectral signatures were captured simultaneously using the OceanView® (Ocean Optics, Inc, Orlando, FL, US) spectroscopy software. Dark current (DC), vignetting and lens distortion were corrected using MIP.

DC remotion from the HS measurements was coded in Matlab® (See Fig. 6). The sun position computed by Pysolar was 77° in azimuth and 75° in elevation, generating a sun-sensor angle of 27.8° (See Fig. 7). From this sun-sensor geometry, results of HS radiance cross-calibration by

band/target assuming a κ-factor of 1/6 are presented in Table 2. Results of reflectance calibration with and without irradiance normalization (Ec. 11) are presented in Table 3.

In Table 3, it can be seen that reflectance estimation error is greater when the HS radiance is not normalized by the downwelling irradiance (option 2, reflectance method) compared to the normalization by the downwelling irradiance (option 1, improved reflectance method).

The geometric factors and error statistics by band are shown in Table 4. It should be noted that there is only one factory calibrated reference panel available, so the reference values $R_{ref}^{target,MS}$ for targets (2), (3) and (4) were extrapolated from (1) and taken as valid after calibration via MIP. For option 2, the estimation error tends to increase as the wavelength moves away from the GRE band to the NIR band while for option 1 the error limit is around 1 to 2%, except for the RED band where a peak of about 9% is present versus 16% of option 2. In both cases, the maximum error values tend to be observed in targets of greater reflectance.

Also, it is important to note that in this setup radiance normalization assuming $\theta_e = \pi/2$ and $\theta_{ss} = 0$ will lead to identical results due to the linear correlation between different reflectance factors and the compensation made by the geometric factor $\tilde{k}_{\Omega}$. However, the effectiveness of the downwelling irradiance correction by the sun-sensor geometry will be valued in flight scenarios of dynamic sensor tilting or where calibrated reflectance targets are not available.

4 Conclusions

This research contributes to the understanding of the state-of-the-art reflectance estimation methodology for industrial multispectral cameras and its extensibility to the calibration of additional low cost hyperspectral sensors, i.e., spectrometers, as there is a gap in the literature on this subject. Special emphasis was placed on the description of the radiometric correction factors associated to the sun-sensor geometry in relation to the BRDF model, so other sensor geometries could be addressed on this basis.

The coefficients of determination found in this setup were superior to 0.999, indicating the suitability of the LRM method to calibrate hyperspectral measurements from the multispectral ones. It was found that multispectral/hyperspectral cross-calibration applying radiance normalization by the downwelling irradiance lead to a reduction of the mean absolute error up to 1:3 with respect to the direct application of the LRM method with no normalization. In particular, the configuration of downwelling light sensor on the top of the UAV found in most agricultural UAVs was studied without consideration of attitude of the multispectral imager.

Nonetheless, this opens the possibility to the analysis of other geometries that could include the relative attitude of the multispectral sensor to the UAV frame, the sun or tilted surfaces. Other important contribution to remark is the use of low-cost spectral sensors used on board the UAV like the Parrot Sequoia and the Ocean Optics STS-VIS, for which scarce literature on radiometric calibration can be found apart from the software development communities on the internet.

The calibration of a low-cost hyperspectral sensor to absolute units of reflectance opens the possibility for the development and adoption and numerous remote sensing applications beyond precision agriculture.

Acknowledgments

The authors thank the support of the Mexican Program for Teaching Professional Development (PRODEP) through grant No. 511-6/18-9344.

References

1. **Aasen, H., Honkavaara, E., Lucieer, A., Zarco-Tejada, P.J. (2018).** Quantitative remote sensing at ultra-high resolution with UAV spectroscopy: A review of sensor technology, measurement procedures, and data correctionworkflows. Remote Sens. Vol. 10, pp. 1–42.
2. **Adão, T., Hruška, J., Pádua, L., Bessa, J., Peres, E., Morais, R., Sousa, J.J. (2017).** Hyperspectral imaging: A review on UAV-based sensors, data processing and

applications for agriculture and forestry. Remote Sens, Vol. 9.

3. **Brezini, S.E., Deville, Y. (2023).** Hyperspectral and Multispectral Image Fusion with Automated Extraction of Image-Based Endmember Bundles and Sparsity-Based Unmixing to Deal with Spectral Variability. Sensors, Vol. 23, 2341.
4. **Burkart, A., Aasen, H., Alonso, L., Menz, G., Bareth, G., Rascher, U. (2015).** Angular dependency of hyperspectral measurements over wheat characterized by a novel UAV based goniometer. Remote Sens.
5. **Burkart, A., Cogliati, S., Schickling, A., Rascher, U. (2014).** A novel UAV-Based ultra-light weight spectrometer for field spectroscopy. IEEE Sens. J. Vol. 14, pp. 62–67.
6. **Chen, W., Wang, H. (2021).** Absolute radiometric calibration and validation of a UAV multispectral sensor: A comparison between the irradiance-based method and reflectance-based method. J. Spat. Sci., Vol. 66, pp. 481–492.
7. **Cohen, Y., Alchanatis, V. (2019).** Spectral and Spatial Methods for Hyperspectral and Thermal Image-Analysis to Estimate Biophysical and Biochemical Properties of Agricultural Crops. Biophys. Biochem. Charact. Plant Species Stud, pp. 73–101.
8. **Cubero-Castan, M., Schneider-Zapp, K., Bellomo, M., Shi, D., Rehak, M., Strecha, C. (2018).** Assessment Of The Radiometric Accuracy In A Target Less Work Flow Using Pix4D Software. In 2018 9th Workshop on Hyperspectral Image and Signal Processing: Evolution in Remote Sensing (WHISPERS), pp. 1–4.
9. **Daniels, L., Eeckhout, E., Wieme, J., Dejaegher, Y., Audenaert, K., Maes, W.H. (2023).** Identifying the Optimal Radiometric Calibration Method for UAV-Based Multispectral Imaging. Remote Sens. Vol. 15, pp. 2909.
10. **Domenzain, L.M., Fallet, C. (2018).** Necessary steps for the systematic calibration of a multispectral imaging system to achieve a targetless workflow in reflectance estimation: A study of Parrot SEQUOIA for precision agriculture. En Messinger, D. W., Velez-Reyes, M. (eds.), Algorithms and Technologies for Multispectral, Hyperspectral, and Ultraspectral Imagery XXIV, pp. 42.
11. **Fenger-Nielsen, R. (2019).** Micasense Image Processing Tutorial (Sequoia). github (rasmusfenger). https://github.com/rasmusfenger/micasense_imageprocessing_sequoia.
12. **Graham, C., Girkin, J., Bourgenot, C. (2022).** Spectral index selection method for remote moisture sensing under challenging illumination conditions. Sci. Rep., Vol. 12, pp. 1–9.
13. **Guo, Y., Senthilnath, J., Wu, W., Zhang, X., Zeng, Z., Huang, H. (2019).** Radiometric calibration for multispectral camera of different imaging conditions mounted on a UAV platform. Sustain.
14. **Hakala, T., Markelin, L., Honkavaara, E., Scott, B., Theocharous, T., Nevalainen, O., Näsi, R., Suomalainen, J., Viljanen, N., Greenwell, C., Fox, N. (2018).** Direct reflectance measurements from drones: Sensor absolute radiometric calibration and system tests for forest reflectance characterization. Sensors (Switzerland), Vol. 18.
15. **Horn, B.K.P., Sjoberg, R.W. (1979).** Calculating the reflectance map. Appl. Opt.
16. **Iqbal, F., Lucieer, A., Barry, K. (2018).** Simplified radiometric calibration for UAS-mounted multispectral sensor. Eur. J. Remote Sens., Vol. 51, pp. 301–313.
17. **Jafarbiglu, H., Pourreza, A. (2023).** Impact of sun-view geometry on canopy spectral reflectance variability. ISPRS J. Photogramm. Remote Sens. Vol. 196, pp. 270–286.
18. **Jakob, S., Zimmermann, R., Gloaguen, R. (2017).** The Need for Accurate Geometric and Radiometric Corrections of Drone-Borne Hyperspectral Data for Mineral Exploration: MEPHySTo-A Toolbox for Pre-Processing Drone-Borne Hyperspectral Data. Remote Sens.
19. **Köppl, C.J., Malureanu, R., Dam-Hansen, C., Wang, S., Jin, H., Barchiesi, S., Serrano**

Sandí, J.M., Muñoz-Carpena, R., Johnson, M., Durán-Quesada, A.M., Bauer-Gottwein, P., McKnight, U.S., Garcia, M. (2021). Hyperspectral reflectance measurements from UAS under intermittent clouds: Correcting irradiance measurements for sensor tilt. Remote Sens. Environ. Vol. 267, 112719.

20. **Kosmopoulos, P. (2024).** Solar irradiance and exploitation of the Sun's power. Planning and Management of Solar Power from Space, pp. 1–20. Elsevier.
21. **Li, H., Song, L., Wang, S., Zhang, H., Zhang, W., Zhao, Y., Huang, Z. (2024).** A method suitable for cross calibration of UAV hyperspectral remote sensors. En Yang, Z. (ed.), AOPC 2024: Optical Spectroscopy and Applications, SPIE, pp. 18.
22. **Li, H., Zhang, H., Zhang, B., Chen, Z., Yang, M., Zhang, Y. (2015).** A Method Suitable for Vicarious Calibration of a UAV Hyperspectral Remote Sensor. IEEE J. Sel. Top. Appl. Earth Obs. Remote Sens., Vol. 8, pp. 3209–3223.
23. **Manfreda, S., McCabe, M.F., Miller, P.E., Lucas, R., Madrigal, V.P., Mallinis, G., Dor, E. B., Helman, D., Estes, L., Ciraolo, G., Müllerová, J., Tauro, F., de Lima, M.I., de Lima, J.L.M.P., Maltese, A., Frances, F., Caylor, K., Kohv, M., Perks, M., Ruiz-Pérez, G., Su, Z., Vico, G., Toth, B. (2018).** On the use of unmanned aerial systems for environmental monitoring. Remote Sens.
24. **Micasense, I. (2022).** MicaSense Camera Image Processing Workflow. MicaSense Knowl.
25. **Micasense, I. (2017).** Micasense Image Processing Tutorial. github (Micasense, Inc.).
26. **Natesan, S., Armenakis, C., Benari, G., Lee, R. (2018).** Use of UAV-Borne Spectrometer for Land Cover Classification. Drones, Vol. 2, pp. 16.
27. **Ocean Optics Inc. (2007).** Ocean Optics catalog 07. Gen. Microtechnology Photonics12.
28. **Olsson, P.O., Vivekar, A., Adler, K., Garcia Millan, V.E., Koc, A., Alamrani, M., Eklundh, L. (2021).** Radiometric correction of multispectral uas images: Evaluating the accuracy of the parrot sequoia camera and sunshine sensor. Remote Sens. Vol. 13, pp. 1–26.
29. **Parrot Drone, S. (2022).** Sequoia documentation. Support Doc. Sequoia.
30. **Peddle, D.R., Peter White, H., Soffer, R.J., Miller, J.R., LeDrew, E.F. (2001).** Reflectance processing of remote sensing spectroradiometer data. Comput. Geosci., Vol. 27, pp. 203–213.
31. **Roosjen, P.P.J., Suomalainen, J.M., Bartholomeus, H.M., Kooistra, L., Clevers, J.G.P.W. (2017).** Mapping reflectance anisotropy of a potato canopy using aerial images acquired with an unmanned aerial vehicle. Remote Sens. Vol. 9.
32. **Samadzadegan, F., Toosi, A., Dadrass Javan, F. (2025).** A critical review on multi-sensor and multi-platform remote sensing data fusion approaches: current status and prospects. Int. J. Remote Sens., Vol. 46, pp. 1327–1402.
33. **Schaepman-Strub, G., Schaepman, M.E., Painter, T.H., Dangel, S., Martonchik, J. V. (2006).** Reflectance quantities in optical remote sensing-definitions and case studies. Remote Sens. Environ.
34. **Schneider-Zapp, K., Cubero-Castan, M., Shi, D., Strecha, C. (2019).** A new method to determine multi-angular reflectance factor from lightweight multispectral cameras with sky sensor in a target-less workflow applicable to UAV. Remote Sens. Environ, Vol. 229, pp. 60–68.
35. **Stow, D., Nichol, C.J., Wade, T., Assmann, J.J., Simpson, G., Helfter, C. (2019).** Illumination geometry and flying height influence surface reflectance and ndvi derived from multispectral UAS imagery. Drones, Vol. 3, pp. 1–28.
36. **Sun, Z., Bu, Z., Lu, S., Omasa, K. (2021).** A General Algorithm of Leaf Chlorophyll Content Estimation for A Wide Range of Plant species. IEEE Trans. Geosci. Remote Sens., 2892.
37. **Wang, Y., Yang, Z., Kootstra, G., Khan, H.A. (2023).** The impact of variable illumination on vegetation indices and evaluation of illumination correction methods on chlorophyll

content estimation using UAV imagery. Plant Methods, Vol. 19, pp. 51.

38. **Yokoya, N., Grohnfeldt, C., Chanussot, J. (2017).** Hyperspectral and Multispectral Data Fusion: A comparative review. IEEE Geosci. Remote Sens. Mag., Vol. 5, pp. 29–56.
39. **Yu, W., Huang, H., Liu, Q., Wang, J. (2024).** Integrating physical model and image simulations to correct topographic effects on surface reflectance. ISPRS J. Photogramm. Remote Sens., Vol. 211, pp. 356–371.
40. **Zeng, C., King, D.J., Richardson, M., Shan, B. (2017).** Fusion of Multispectral Imagery and Spectrometer Data in UAV Remote Sensing. Remote Sens., Vol. 9, pp. 696.

Article received on 06/06/2025; accepted on 05/10/2025.
**Corresponding author is Azgad Casiano Ramos.*